



TITLE:

Study of dynamic stability of unsaturated embankments with different water contents by centrifugal model tests

AUTHOR(S):

Higo, Yosuke; Lee, Chung-Won; Doi, Tatsuya;
Kinugawa, Teppei; Kimura, Makoto; Kimoto, Sayuri;
Oka, Fusao

CITATION:

Higo, Yosuke ...[et al]. Study of dynamic stability of unsaturated embankments with different water contents by centrifugal model tests. *Soils and Foundations* 2015, 55(1): 112-126

ISSUE DATE:

2015-02

URL:

<http://hdl.handle.net/2433/197441>

RIGHT:

© 2015 Japanese Geotechnical Society. Production and hosting by Elsevier B.V. NOTICE: this is the author's version of a work that was accepted for publication in *Soils and Foundations*. Changes resulting from the publishing process, such as peer review, editing, corrections, structural formatting, and other quality control mechanisms may not be reflected in this document. Changes may have been made to this work since it was submitted for publication. A definitive version was subsequently published in *Soils and Foundations*, 55(1), 2015, doi:10.1016/j.sandf.2014.12.009; This is not the published version. Please cite only the published version.; この論文は出版社版ではありません。引用の際には出版社版をご確認ください。

Study of dynamic stability of unsaturated embankments with different water contents by
centrifugal model tests

Yosuke HIGO*, Chung-Won LEE**, Tatsuya DOI**, Teppei KINUGAWA**, Makoto
KIMURA***, Sayuri KIMOTO*** and Fusao OKA****

*Department of Urban Management, Kyoto University, Japan

** Former Student of Department of Civil and Earth Resources Engineering, Kyoto University

*** Department of Civil and Earth Resources Engineering, Kyoto University

**** Professor Emeritus, Kyoto University

Abstract: It has been pointed out that the damage to unsaturated embankments caused by earthquakes is attributed to the high water content brought about by the seepage of the underground water and/or rainfall infiltration. It is important to study the effects of the water content on the dynamic stability and deformation mode of unsaturated embankments in order to develop a proper design scheme, including effective reinforcements, for preventing severe damage. This paper presents a series of dynamic centrifugal model tests with different water contents to investigate the effect of the water content on the deformation and failure behaviors of unsaturated embankments. By measuring the displacement, the pore water pressure and the acceleration during dynamic loading, as well as the initial suction level, the dynamic behavior of unsaturated embankments with an approximately optimum water content, a higher than optimum water content and a lower than optimum water content, are discussed. In addition, an image analysis reveals the displacement field and the distribution of strain in the embankment, by which the deformation mode of the embankment with the higher water content is clarified. It is found that in the case of the higher water content, the settlement of the crown

is large mainly due to the volume compression underneath the crown, while the small confining pressure at the toe and near the slope surface induces large shear deformation with volume expansion.

Keywords: unsaturated soil, embankment, centrifugal model test, water content, dynamic loading

1. Introduction

The seismic vulnerability of road embankments has been recognized as an important geotechnical problem. In past earthquakes, road embankments have experienced catastrophic failures. A recent example is the collapse of highway embankments caused by the 2011 off the Pacific coast of Tohoku earthquake on March 11, 2011. In addition, the road embankments constructed on mountain/hill sides were severely damaged by the 2009 Suruga-bay earthquake, the 2007 Noto Hanto earthquake and the 2004 Niigata-ken Chuetsu earthquake (e.g., NILIM and PWRI 2004, 2011; NILIM, PWRI and BRI 2008; Central Nippon Expressway, Co. Ltd. 2009). The collapse of road embankments is a very important issue since the fragmentation of road transportation disables the supply of relief materials and the carrying of injured persons, and also induces the isolation of villages.

It has been pointed out that the road embankments severely damaged during these past earthquakes contained a great deal of water due to seepage water or rainfalls. In particular, embankments constructed on valley-like topographies are apt to allow the underground water to flow into embankments. In the cases of the Noto Hanto earthquake and the Niigata-ken Chuetsu earthquake, the seepage water flow and the high water content are possible reasons for the damage (e.g., Sasaki et al. 2008). This suggests that the effect of the seepage water flow and the high water content in embankments on the dynamic failure of road embankments has to be studied in detail.

Recently, many researchers have tried to study the dynamic stability of unsaturated embankments by taking into account the water content history via centrifugal model tests (e.g., Hayashi et al. 2002,

Matsuo et al. 2002, and Ohkawa et al. 2008, Okamura et al. 2013). The aim of most of these studies has been to reveal the effect of the increase in water content on the amount of deformation. This is because the displacement, such as the settlement of the crown, is crucial for road embankments as an infrastructure in the engineering sense. It is important, however, to know the deformation modes of unsaturated embankments in order to properly evaluate the seismic stability and to propose effective reinforcement methods. From this point of view, and to the authors' knowledge, there have been only a limited number of such studies.

In addition, a physical interpretation of the dynamic behavior of unsaturated embankments has rarely been reported because the physical modelling of unsaturated soils is more complicated than that of fully saturated soils in terms of the similarity rules for suction and the distribution of water contents. There have been publications on static deformation and strength characteristics, including oedometric tests (Thorel et al. 2013) and capillary rises (Rezzoug et al. 2000; Esposit 2000; Okamura and Tamamura 2011) under centrifugal conditions. They have revealed that the suction level and the distribution of water contents in a prototype scale are almost independent of centrifugal acceleration. It is necessary, however, to study further the deformation and failure characteristics of unsaturated soils subjected to dynamic loading based on the findings obtained under static conditions.

In this study, dynamic centrifugal model tests on unsaturated road embankments with different water contents are conducted in order to clarify the relation between the dynamic stability of road embankments and the water content history of the embankments. Embankments are generally constructed by compaction with an approximately optimum or slightly higher than optimum water content. It is known that unsaturated embankments exhibit the highest strength with a slightly lower water content owing to the effect of suction. When the embankments are subjected to an increase in groundwater level and/or infiltration of water from the surface, due to rainfalls or seepage flow, the water content of the embankments increases and the suction eventually decreases. The post-survey by

Sasaki et al. (2008) on the 2007 Noto Hanto earthquake provides that a higher water content due to the large fines content and higher levels of groundwater inside the embankments were observed in the largely deformed embankments. Hence, we have conducted tests with three different water contents, namely, an approximately optimum water content, a lower than optimum water content, and a higher than optimum water content.

Dynamic input motion has been applied to the model embankments in a centrifugal acceleration field of 50 G. Through the measurement results for the displacement, the pore water pressure and the acceleration response, and the distribution of displacement and strain provided by the image analysis with the particle tracking velocimetry (PTV) technique, the dynamic behaviors of the unsaturated embankments with different water contents have been studied.

2. Testing Method and Soil

2.1 Geotechnical centrifuge

In this study, the geotechnical centrifuge at the Disaster Prevention Research Institute (DPRI), Kyoto University, has been used. Figure 1 and Table 1 show the schematic figure and the specifications of this apparatus, respectively. The effective rotation radius, defined as the length from the rotation axis of the arm to the center of the model, is 2.5 ± 0.05 m. The maximum centrifugal accelerations are 200 g and 50 G when using a shaking table.

Dynamic loading is applied unidirectionally to the model through a shaking table by the servo hydraulic actuator shown in Figure 2. Specifications of the shaking table are listed in Table 2. Dynamic loading is applied by adjusting the inflow rate of the oil to the piston from the accumulator tank by controlling the servo hydraulic valve. The input motion of the shaking table is conducted through a displacement control system. Hence, the acceleration of the input dynamic loading was measured by the accelerometer installed directly on the shaking table.

97

98 2.2 Soil

99 The test sample used in this study is Yodogawa-levee sand sieved to a diameter of less than 2.0
100 mm; this soil material is classified as an SF according to the Unified Soil Classification System of
101 Japan. Yodogawa-levee sand has been used to repair the embankments of the Yodo River in the Kansai
102 area. The material properties, the grain size cumulative curve and the compaction curve of Yodogawa-
103 levee sand are shown in Table 3, Figure 3 and Figure 4, respectively.

104

105 2.3 Model setting

106 The model container, the model configuration and the sensor locations are illustrated in Figure 5.
107 For simplicity, the accelerometers, the pore water pressure transducers and the laser displacement
108 sensors are referred to as “A”, “P” and “L”, respectively. The model container is basically made of
109 aluminum, except for the front surface of polycarbonate plastic, through which we can view the model
110 embankment during the tests, even when the centrifugal machine is active, using a video camera
111 installed on the arm of the centrifugal machine.

112 This model simulates an embankment constructed on a stiff ground such as a mountains area. This
113 is done because the embankments constructed on the boundary of cutting and filling were more
114 severely damaged by past earthquakes (e.g., NILIM and PWRI 2008). The width and the thickness of
115 the foundation ground are 45 cm and 6 cm, respectively. The width of the crest of the embankment is
116 5 cm and the height is 10 cm. The inclination of the embankment is 1:1.8 based on the guidelines for
117 road earthwork and embankment construction (Japan Road Association 2010).

118 The centrifugal acceleration used in this study is 50 G. Thus, in the prototype scale, the width of
119 the crest is 2.5 m, the height is 5 m and the length is 7.5 m. As for the foundation ground, the width
120 and the thickness of the base ground are 22.5 m and 3 m, respectively.

Prior to preparing the model embankment, test samples were mixed with water to attain the prescribed initial water contents. Then, the model embankments were prepared in eight layers by the compacting method. The foundation ground and the embankment were separated into three layers (thickness: 30 mm, 15 mm and 15 mm), and five layers (even thickness of 20 mm), respectively. The degree of compaction D_c for all the cases was set to be 91% ($\rho_d=1.675 \text{ g/cm}^3$). D_c is determined by the volume and the weight of the soil in each layer.

The procedure for the construction of the model embankment is shown as follows:

- (1) Put the soil-water mixture into the model container uniformly and compact the soil to the prescribed volume corresponding to a D_c of 91%.
- (2) For the image analysis explained later, insert the targets, which are 5.0 mm in diameter and 5.0 mm in thickness, evenly spaced at 2.5 cm along the front transparent wall of polycarbonate.
- (3) After the compaction of each layer, scarify the top surface to improve the connectivity between the layers.
- (4) Embed the accelerometers and the pore water pressure transducers at the prescribed locations.
- (5) Repeat steps (1) through (4), and the construction of the foundation ground will be complete.
- (6) Compact each layer of the embankment using the formworks shown in Figure 6(a).
- (7) After removing the formworks, cut out the extra soil (Figure 6(b)).

Pendulum-type accelerometers (produced by SSK, Co., Ltd., A6H-50) and the double diaphragm type of pore water pressure transducers (produced by SSK, Co., Ltd., P306-A) are used. The accelerometers are 6 mm cubed. The pore water pressure transducers are 8 mm in diameter and 6 mm in height. The displacements of the model embankment are measured at the crown and the toe of the embankment by the laser displacement sensors (produced by KEYENCE, Corporation), for which the aluminum target plates with white lacquer were installed on the model embankment.

2.4 Pore fluid

In the centrifugal model tests, considering both fluid flow and dynamic motion, a viscous fluid is generally used as a substitute pore fluid in order to compensate for the difference in similarity rules between fluid flow behavior and dynamic behavior. As for the viscous fluid, the metolose solution (methylcellulose) has been commonly used since the density of the solution is almost the same as that of water and users can easily adjust the viscous coefficient. In the case of fully saturated soils, it is known that the mechanical characteristics of soils, such as strength and stiffness, are not affected by the metolose solution (Dewoolker et al. 1999). On the other hand, in the case of unsaturated soils, the suction level is definitely affected by the metolose solution whose surface tension is less than that of water. For example, the surface tension of the metolose (SM100 produced by Shin-Etsu Chemical Co., Ltd.) solution, with a concentration of 0.2% at 20°C, is about 54×10^{-3} N/m (Metolose Brochure 2007), which is less than that of water with a concentration of 72.75×10^{-3} N/m (National Astronomical Observatory 2001). Ko and Dewoolker (1999) also pointed out the decrease in surface tension by the metolose solution, and Okamura and Tamamura (2011) reported that the capillary rise in the metolose solution, with a viscosity 40 times that of water, is less than that of water.

In the present study, water was used as the pore fluid in order to avoid a reduction in suction and to correctly evaluate the effect of suction on the deformation of the embankments. Meanwhile, when water is used as the pore fluid, the permeability coefficient is N times larger in a centrifugal field of NG . The saturated permeability of Yodogawa-levee sand is 4.79×10^{-6} m/sec when the dry density is 1.675 g/cm^3 . Thus, the permeability coefficient could be 2.40×10^{-4} m/sec under the centrifugal acceleration of 50 G. This permeability coefficient is larger compared to general embankment materials, but is still within the range of permeability for road embankments. For example, the permeability of the gravelly soil from the coastal terrace for the road embankment damaged in the 2009 Suruga-bay earthquake is 3.67×10^{-4} m/sec (Nakamura et al. 2010).

2.5 Image analysis

In order to quantify the displacement field, an image analysis was conducted based on the particle tracking velocimetry (PTV) technique. The image analysis method used in this study is similar to that by Kodaka et al. (2001) and Higo et al. (2006).

We took digital photographs before and after the tests. Then, meshes were drawn by employing the center of the targets as the nodes of the meshes from those photographs. After digitizing the coordination of the nodes from the photographs before and after the tests, the nodal displacements were measured by the distance between the nodes before and after the tests. On the bottom and the both sides boundary, since we could not install the targets, we assumed that the points on the boundary were fixed, i.e., the displacements of the nodes on the boundaries are zero. Finally, adopting the B matrix for the four-node or the three-node isoparametric finite elements provides the strain tensor for each element, $\{\varepsilon\}$, namely,

$$\{\varepsilon\} = [B]\{u\} \quad (2.1)$$

in which,

$$\{\varepsilon\}^T = \{\varepsilon_{xx}, \varepsilon_{yy}, 2\varepsilon_{xy}\} \quad (2.2)$$

$$\{u\} = \{u_x^1, u_y^1, u_x^2, u_y^2, u_x^3, u_y^3, u_x^4, u_y^4\} \quad (2.3)$$

where, $\{u\}$ is the nodal displacement vector and subscripts x and y denote horizontal and vertical directions. ε_{xx} , ε_{yy} and ε_{xy} are the horizontal, vertical and shear strain components, respectively. The superscripted numbers (1 to 4: four-node elements and 1 to 3: three-node elements) indicate the nodal numbers of the isoparametric elements.

The deviatoric strain vector $\{e\}$ can be given as

$$\{e\}^T = \{e_{xx}, e_{yy}, e_{xy}\} = \{\varepsilon_{xx} - \frac{\varepsilon_v}{2}, \varepsilon_{yy} - \frac{\varepsilon_v}{2}, \varepsilon_{xy}\} \quad (2.4)$$

in which, $\varepsilon_v (= \varepsilon_{xx} + \varepsilon_{yy})$ is the volumetric strain in a two-dimensional form.

In this study, the shear strain is defined as the second invariant of the deviatoric strain tensor as follows:

$$\gamma = \sqrt{e_{xx}^2 + e_{yy}^2 + 2e_{xy}^2} \quad (2.5)$$

It should be noted that the photos, both before and after the tests, are taken under the gravitational field. This is because the resolution of the photos taken under the 50 G field, using a digital video camera installed on the arm of the centrifugal machine, is not high enough to distinguish all the target points. The settlement and the rebound, due to the changes in acceleration from 1 G to 50 G and 50 G to 1 G, respectively, probably influence the results of the image analysis. The effect on the obtained displacement, however, would be negligible because the displacements caused by the changes from 1 G to 50 G and 50 G to 1 G are probably almost the same.

3. Testing Program

3.1 Test cases

The test cases are listed in Table 4. The water content “before compacting”, w_{bef} , indicates that of the soil samples prior to compacting. The average water contents measured “after testing”, w_{aft} , are also listed in Table 4. The locations of the measurements are shown in Figure 7. The water contents after testing in Cases 1, 2 and 3 were smaller than those before compacting. This is because the water content decreases by 1% to 1.5% due to the unavoidable evaporation during the whole procedure of the tests over a period of about 8 hours. However, w_{aft} could be fairly similar to the water content during dynamic testing, since the sampling was performed quickly, in about 40 minutes, after the end of the test. Consequently, the water content during testing in Case 2, 13.5%, is nearly equal to the optimum water content, w_{opt} , of 13.7%, while the water contents of Cases 1 and 3 were the lower and higher than optimum water contents of 12.1% and 17.4%, respectively.

In general, embankments are compacted with about the optimum water content or a slightly higher water content, as employed in Case 2. The noticeably higher water content used in Case 3 is aimed at an embankment with the infiltration of water after construction, which makes the embankment weaker. In Case 1, the lower water content involves higher suction than that of the optimum one, which strengthens the embankment. Through a comparison among these three cases, the effect of the water content on the dynamic stability of embankments has been studied.

3.2 Water content

Distributions of water contents were measured after the tests under the 1 G field and the contours have been drawn in Figure 8. It took 9 minutes to stop the centrifugal machine, from 50 G to 1 G, and then, after about 30 minutes, the data sampling for the measurement was done. According to the test results by Esposito (2000), the distribution of water contents does not change significantly, even after the centrifugation has stopped and the acceleration has decreased to the 1 G field. Consequently, the distribution of water contents shown in Figure 8 is almost identical to that in the 50 G field with the deformation due to dynamic loading.

As for the distribution of water contents for each case at the initial state, just before dynamic loading, it must be different from that after testing, as shown in Figure 8. In particular, in Case 3, the initial distribution is probably much different from that after the test, since a very large deformation occurs due to the dynamic loading (see Figure 11 later). This rather heterogeneous distribution of water contents in Case 3 probably depends on the changes in soil volume and/or the distribution of trapped air and/or the flows of pore water and pore air. For example, the noticeably larger than average water content at the toe is possibly because the positive dilatancy, which will be discussed later, causes the soil to expand and to induce the water inflow from the other parts. Larger water contents are also seen near both side boundaries probably due to the rather higher permeability between the soil and the wall.

On the other hand, the initial distributions of water contents for Cases 1 and 2 are similar to those after the test because the deformation is not significant (see Figure 11 later). Nevertheless, the initial water content at each point in the embankment in Case 3 is much larger than that in Cases 1 and 2, and that in Case 2 is larger than that in Case 1.

It should be noted that the embankment in Case 3 was not fully saturated, but could be partly saturated because most of the measured water contents are lower than the water content of the fully saturated one of 22.1%, which is calculated using the initial void ratio e_0 of 0.589 and ρ_s of 2.661 g/cm³, i.e., no volume change is assumed.

3.3 Suction

The relation between the degree of saturation S_r and the suction for the Yodagawa-levee sand is shown in Figure 9. The compacted Yodogawa-levee soil specimens were prepared in the mould for the conventional compaction tests with almost the same D_c of 91%. Each specimen has a different S_r , ranging from 47% to 80%, for which we have measured the suction levels using a tensiometer.

Using w_{aft} , a e_0 of 0.589 and a ρ_s of 2.661 g/cm³, the average degrees of saturation for Cases 1, 2, and 3 are calculated to be 54.5%, 61.2% and 78.7%, respectively. According to Figure 9, the initial suction in Case 1 is about 17 kPa, which is larger than that in the other two cases: 7 kPa in Case 2 and almost zero in Case 3. Corresponding to the distribution of the water contents, the suction levels at the upper parts are larger than those at the lower parts. Hence, even in Case 3, the soil in the vicinity of the surface, e.g., at the crest, with a lower water content of 15.5%, which corresponds to the degree of saturation of 70%, has small suction according to Figure 8.

It is known that the suction in the NG field could be the same as that under the 1 G field in cases where the pore sizes are small and the influence of gravity on the capillary force is not significant (Heibrock and Rezzoug 1998). Other experimental studies have shown that the capillary rise in a

prototype scale is independent of the centrifugal accelerations until 40 G when using relatively fine sand, e.g., Congleton sand with a D_{50} of 0.12 mm by Rezzoug et al. (2000) and silty sand with a D_{50} of about 0.07 mm by Okamura and Tamamura (2011). The Yodogawa-levee sand used in this study has a D_{50} of 0.28 mm and a fines content of 26%. The centrifugal acceleration of 50 G is a little larger, but not very different from 40 G. Thus, the suction of the Yodogawa-levee sand under a 50 G field is probably similar to that measured under the 1G field. Additionally, this could be confirmed because the deformation of the case with a lower water content is much smaller than that with a higher one, as will be mentioned later.

3.4 Input motion

In all cases, tapered sinusoidal waves with a frequency of 1 Hz (50 Hz in the model) were used as input waves, and the duration of the waves was 30 sec (0.6 sec in the model). The amplitudes of the waves for each case are listed in Table 4. The input waveform of the displacement-control shaking table is shown in Figure 10(a), and the acceleration waveforms consequently measured at the shaking table for all cases are shown in Figure 10(b). Hereinafter, “input wave” indicates the acceleration wave measured at the shaking table.

The duration and the frequency of the input wave are similar to the observed near-field earthquake with respect to the predominant period. For example, in the 1995 Hyogoken-Nanbu earthquake, the predominant period at JR Takatori was about 1 or 2 seconds and the duration of the main shock was about 20 seconds (e.g., Sakai 2009).

3.5 Testing procedure

The model embankment was prepared by the compaction method. During the construction, measuring instruments were installed at the prescribed locations, as shown in Figure 5. Four

accelerometers were embedded near the surface and inside the model embankment. Four pore water pressure transducers were embedded in the foundation ground and two pore water pressure transducers were embedded in the embankment. After the construction of the embankment, the laser displacement sensors and the target plates were installed for measuring the horizontal and vertical displacements at the toe of the slope and the vertical displacement of the crest. The sampling interval was 0.01 seconds (0.2 milliseconds in the model) employed in the dynamic loading process.

After preparing the model embankment with the installation of measuring instruments, the model container was placed on the shaking table of the centrifugal machine. The centrifugal acceleration gradually increased up to 50 G spending about 12 minutes in the model scale. The input wave was applied for five minutes in the model scale, after the centrifugal acceleration had reached 50 G, in order to ensure the convergence of the deformation caused by the centrifugal acceleration.

4. Test Results

In the test results described in this section, the directions of the displacements and the acceleration are indicated in each figure. Basically, the left side of the figures corresponds to the minus values and vice versa. For the volumetric strain, the compression is positive.

4.1 Deformation

Figure 11 shows the displacements measured by the laser displacement sensors, and the distribution of the displacement vectors obtained by the image analysis for each case. Note that the displacements during the dynamic motion do not include those occurring before shaking due to the centrifugal acceleration indicated by ‘displacements before shaking’.

4.1.1 Deformation before dynamic loading

We measured the displacements induced by the centrifugal acceleration of 50 G just before applying dynamic loading. The displacements in Case 1 are almost zero, while larger displacements are observed in Cases 2 and 3. In particular, both the settlement and the displacements at the toe are rather significant in Case 3. The difference in the displacements among the three cases is attributed to their own weight as well as to the suction levels, i.e., higher suction contributes to increases in stiffness, since the degrees of compaction are the same.

4.1.2 Deformation during dynamic loading process

For all the cases, the displacements increase from the beginning of shaking and gradually accumulate until the end of shaking, i.e., at 30 seconds. After the shaking, the displacements become negligibly small.

In Case 1, the horizontal displacement at the toe to the left, the settlement at the toe and the settlement at the crest are finally observed. The directions of the displacements in Case 2 are the same as those in Case 1, but the final displacements are slightly larger than those in Case 1.

In Case 3, on the other hand, the crest is largely displaced vertically downward. The settlement at the crest, at the end of the input motion, is 334.3 mm. In the meantime, the horizontal displacement at the toe of the embankment is finally 438.0 mm to the left. It should be noted that the target plate was largely displaced with soil and eventually the measured displacement at L3 increased to the upper limit of the laser displacement transducer. Namely, the horizontal displacement at the toe must be larger than 438.0 mm. Thus, we employed the displacement obtained by the image analysis, of 647.8 mm, as the final horizontal displacement at the toe. The vertical displacement at the toe progresses downward for a period of 20 seconds, and then turns upward. Finally, the vertical displacement is 6.4 mm upward at the end of the input motion. In addition, cyclic deformation can be observed at the toe both horizontally and vertically, while the displacement at the crest is not oscillated.

Figure 12 demonstrates the distributions of shear strain γ and volumetric strain ε_v obtained by the image analysis. It is seen that both the shear and the volumetric strain levels in Case 3 are obviously larger than the others. In addition, the strain levels in Case 2 are a little larger than those in Case 1.

It is seen in Case 1 that relatively large shear strain is observed at both the top of the slope and the toe of the slope. In Case 2, larger shear strain is also seen at the top of the slope. The shear strain is rather small at the toe, but is relatively large at the slope just next to the toe. Larger shear strain can also be seen in the embankment beneath the crest in both Cases 1 and 2. The embankments in Cases 1 and 2 exhibit similar distributions of shear strain. On the other hand, in the case of a higher water content, Case 3, the largest shear strain is observed at the toe, and shear strain localization is seen to pass through the toe and underneath the crest.

At the slope in all cases, the expansive volumetric strain can be seen in the same place where shear strain is observed. Hence, positive dilatancy occurs. The expansive volumetric strain levels of Case 3 are much larger than those of the other two cases. Let us discuss the dilatancy behavior seen in Case 3. In particular, the obvious dilatancy behavior can be seen in the localization zone of shear strain of Case 3 since the volumetric strain in the localization zone is expansive. On the other hand, very large volume compression can be seen widely beneath the crest. This volume compression is consistent with the large subsidence of the crest. Large volume compression can also be observed in the localization zone, in which negative dilatancy occurs.

Furthermore, the shear strain levels near the left boundary are relatively high, at which rather large volumetric compression is also observed. This is because the soils in this part are compressed by the left side wall and the deformation of the embankment in the left direction.

4.2 Pore water pressure

Figure 13 shows the time histories of the pore water pressure for the three cases at each measuring point along with the distributions of shear strain and volumetric strain for Case 3 with the transducer locations.

4.2.1 Pore water pressure before dynamic loading

At first, let us focus on the pore water pressure levels at the initial state, i.e., just before applying the dynamic load under the centrifugal acceleration field of 50 G. It is seen that the initial pore water pressure levels in Cases 1 and 2 are almost zero, while those in Case 3 are positive and higher than the others. The pore water pressures in the model embankments for Cases 1 and 2 are probably negative, i.e., suction, that could not be measured by the transducers because zero air-entry filters were used for the transducers. On the other hand, the initial pore water pressures measured in Case 3 are positive, which suggests that the model embankment was partly saturated, in particular around the transducers. In other words, the model embankment for Case 3 was not fully saturated, but was unsaturated probably in the insular-air saturation regime, since the suction level corresponding to the water content in Case 3 (see Figure 9) is almost zero and the water content is lower than that for fully saturated soils.

4.2.2 Dynamic loading process

The pore water pressures in Cases 1 and 2 remain almost zero. The very small pore water pressures in Cases 1 and 2 indicate that the difference in displacements between Cases 1 and 2 is mainly attributed to the difference in suction levels between the two cases. On the other hand, the pore water pressures of Case 3 change largely at all of the measuring points. The pore water pressure levels at P2 and P4 increase, and those at P1 and P5 increase even more significantly.

It is seen in the distribution of volumetric strain that larger volume compression occurs around P1 and P5 where the larger increase in pore water pressure is observed. The slight increase at P2 and P4

probably corresponds to the small volume compression in the vicinity of P2 and P4. However, small expansive volumetric strain is observed at P2 and P4. This is because of the coarse mesh of the target points and of the slight difference in deformation between the place of the target point at the front wall and the place of the pore pressure transducers in the middle of the two walls.

The pore water pressure at P6 increases at the beginning of the input motion, and then decreases after about 5 seconds. Positive dilatancy significantly occurs around P6, since the larger shear strain with expansive volumetric strain is observed there. The pore water pressure of P3 also decreases, but the decrement is much smaller than that of P6, even though the expansive volumetric strain at P3 is comparable to that at P6. This is probably because the pore water flowing into P3, associated with the volume expansion, from somewhere in the upper portions, e.g., the voids around P6.

In addition, it can be seen that the pore water pressure levels at P3, P4, P5 and P6 in Case 3 are oscillated largely, at which large shear strain can be seen. The increase and the decrease in pore water pressure are related to negative dilatancy and positive dilatancy, respectively.

The maximum pore water pressure at P6 in Case 3 was 25 kPa. The initial overburden pressure at P6 can be calculated to be 38.6 kPa by using a wet soil unit weight of 19.3 kN/m³ (obtained with an initial void ratio of 0.589, an initial degree of saturation of 0.814 and a particle density 2.661 g/cm³) and an overburden thickness of 2.0 m. Consequently, the maximum pore water pressure is smaller than the initial overburden pressure. In the same manner, it is confirmed that the pore water pressure of the other measuring points is smaller than the initial overburden pressure. In addition, sand boils were not observed at the surface of the embankment after the tests. Hence, the stress of the soil skeleton decreased due to the positive pore water pressure, but liquefaction probably did not occur in Case 3.

After 30 seconds, it is seen that the pore water pressure levels at P1, P2 and P5 dissipate gradually. The pore water pressure of P6 at 30 seconds becomes smaller than the initial value and gradually decreases even further after dynamic loading. This suggests that the pore water around P6 flows out

to the lower parts.

4.3 Acceleration response

Figure 14 shows the acceleration responses measured at the crest, A1, beneath the crest, A2, at the toe, A3, and in the embankment close to the toe, A4. In all cases, the amplitude of the acceleration response of A1 is larger than that of A2 which is larger than the input wave. Namely, the input wave was more amplified toward the upper part, which is consistent with the amplification of waves for linear elastic bodies based on the multiple reflection theory, although in Case 3 significant plastic deformation probably occurred in the embankment, i.e., the elastic stiffness may be nonlinear. It is seen that the larger amplification occurs in the embankments with the higher water contents. This suggests that the shear elastic stiffness with the higher water contents is smaller, which leads to the smaller impedance ratio.

The responses at A3 and A4 for Case 1 and Case 2 are larger than the input waves, and the amplitude of A4 is a little larger than that of A3. This is probably because the higher location of A4 than A3 results in the larger amplification. It is seen that the response of A3 is asymmetric, namely, the negative amplitude is much larger than the positive one. The embankment is displaced in the left direction, i.e., the displacement is negative, caused by the input motion in the left direction, and the largest horizontal displacement is observed at the toe where A3 is installed. On the other hand, positive displacement, caused by the input motion in the right direction, is much smaller than the negative one. This large deformation corresponds to the fact that the acceleration response in the left direction is much larger than that in the right direction.

5. Discussions

5.1 Deformation mode of embankment with approximate optimum water content and lower water content

As seen in the results for Case 1 and Case 2, the deformation of the embankments with approximately optimum or lower than optimum water contents is limited and not significant, and the pore water pressure levels change little during the dynamic loading. It can be seen in the distribution of strain, however, that both cases exhibit a similar mode. Namely, relatively large shear strain can be observed along the slope including the top in Case 1 and Case 2. The volumetric strain levels for these two cases are very small, but it seems that the strain close to the surface is expansive, i.e., positive dilatancy occurs. These behaviors close to the surface and at the toe are probably caused by the relatively lower overburden confining pressure, at which the larger stress ratio has been induced by the dynamic shear loading.

In addition, relatively larger shear strain is also seen beneath the crest in both cases, where the compressive volumetric strain is observed. The compression attributes to the subsidence of the crest, and this mode is more significantly seen in Case 3 with higher water contents.

The subsidence and the volumetric strain in Case 1 are smaller than those in Case 2. This means that the larger suction in the case of a lower water content more effectively sustains the original shape, excluding the small shear deformation at the slope and the toe.

5.2 Deformation mode of embankment with higher water content

The embankment with the higher water content in Case 3 exhibits much larger deformation and pore water pressure than the other cases. The main reason for the larger deformation is the suction of almost zero and the increase in pore water pressure. Since the embankment with the higher water content is partly saturated, the positive pore water pressure is observed where the suction levels are zero. Pore water pressure increases during dynamic loading at which time volume compression occurs.

The increase in pore water pressure decreases the stress of the soil skeleton, which enhances the deformation of the embankment.

The deformation mode of the embankment in Case 3 is schematically illustrated and the distribution of strain components, horizontal strain component ε_{xx} , vertical strain component ε_{yy} , shear strain component ε_{xy} , shear strain γ and volumetric strain ε_v are shown in Figure 15. The largest γ is observed at the toe and a relatively large γ can be seen close to the surface of the slope and the foundation ground. In addition, the localization of γ can be seen from the toe to the lower part of the crest. As for the changes in volume, large expansive strain is observed at the toe, along the slope and on the surface of the foundation ground just to the left of the toe. Namely, positive dilatancy occurs at the toe and on the surface close to the toe of the embankment, where the overburden confining pressure is relatively small. In particular, the obvious positive dilatancy can be seen in the localization zone.

On the other hand, the large volume compression can be observed at the lower part of the crest, where shear strain γ can also be seen. Although the strain levels and the displacement are much smaller in Case 2 than in Case 3, compressive volumetric strain is also seen in the same place and the crest settles down. This suggests that cyclic shear loading induces volume compression beneath the crest, where the overburden confining pressure is relatively large. In particular, much larger compression occurs in the case of the lower suction levels of the embankment with higher water contents. The compression in the embankment with a high degree of saturation results in the increase in pore water pressure. The pore water pressure decreases the stress of the soil skeleton, which enhances the large deformation.

As shown above, we have observed two typical types of deformation in the embankment with a higher water content: (i) shear deformation with positive dilatancy localized at the toe and beneath the slope surface and (ii) large compression underneath the crest with shear strain inducing the subsidence of the crest. In the area with large compression underneath the crest, it is seen that vertical strain ε_y

and horizontal strain ε_x are large, while shear strain component ε_{xy} is small. On the other hand, ε_{xy} is large in the area close to the toe. This suggests that the deformation mode close to the toe is similar to direct shear with positive dilatancy, while the deformation mode underneath the crest is like triaxial compression, i.e., indirect shear deformation.

The shear strain localization is seen to be similar to the circular slip failure mode that has been widely known as a failure mode of embankments. Through the measurement of the pore water pressure and the image analysis, it has been found that the failure mode is attributed to shear deformation with positive dilatancy near the slope surface, including the toe and the shear deformation with large volume compression, i.e., negative dilatancy, beneath the crown. In particular, the settlement of the crown is mainly due to the volume compression which occurs under relatively large levels of confining pressure in deeper parts, while the small levels of confining pressure at the toe and near the slope surface involve large shear deformation with volume expansion.

Here, let us discuss the boundary effect on the deformation mode. Shear strain and compressive volumetric strain can be observed at the left boundary, which suggests that the left boundary might restrain ground movement. We prepared the foundation ground to be as wide as possible, but it is impossible to completely avoid the boundary effect because of the limitation of the present centrifugal model test apparatus. It is worth mentioning, however, that the obtained deformation mode is fairly similar to the failure mode observed in reality, e.g., the collapse of a road embankment caused by the 2007 Noto Hanto earthquake (NILIM, PWRI and BRI, 2008), in which the failure plain passes through the crown and the foundation ground just close to the toe of the embankment. This fact supports the deformation mode obtained in the present study, but it is still desirable to ensure the influence of the boundary effect, for which numerical simulations and extra experiments with larger model containers could be effective.

6. Conclusions

Dynamic centrifugal model tests for well-compacted unsaturated embankments with the approximately optimum water content and lower and higher than optimum water contents, have been carried out. The degrees of compaction for all the cases are the same. The embankment with the higher water content was in the regime of insular-air saturation whose suction level was almost zero. The input motion was a simple sinusoidal wave.

The deformation of both the embankment with the approximately optimum water content and that with the lower than optimum water content was small. In particular, the deformation of the latter with higher suction level was smaller. During dynamic loading, the pore water pressure changed little. Although the deformation was small, it was found that the shear strain with positive dilatancy at the surface of the slope, including the toe and the shear strain with negative dilatancy underneath the crown, could be observed.

On the other hand, the embankment with the higher than optimum water content exhibited very large deformation. This is mainly because of the almost zero suction and the increase in pore water pressure. The measurement of the pore water pressure and the displacement, as well as the image analysis, have revealed the deformation mode of the embankment with the higher water content:

- (1) Shear strain localized from the toe to the lower part of the crest.
- (2) Large volume compression occurred underneath the crest where the pore water pressure increased. This compressive deformation is attributed to the large settlement of the crest as well as the shear deformation with negative dilatancy.
- (3) Shear deformation with large volume expansion, i.e., positive dilatancy, occurred at the toe and the surface of the slope, where the pore water pressure decreased.

Volume compression can be observed at a rather deep part under the higher confining pressure, where negative dilatancy occurs. On the other hand, the soils close to the surface under lower confining

pressure exhibit volume expansion, where positive dilatancy occurs.

The acceleration response is amplified as in the upper part and/or the part close to the surface. In the case of a higher water content, the amplification is larger than in the cases with the optimum and lower water contents.

Acknowledgment

This research was supported in part by the National Institute for Land and Infrastructure Management, MLIT, Japan (grant for the research and development of technologies for improving the quality of road policies, No. 21-4, 2009-2012).

References

- Central Nippon Expressway, Co. Ltd., Handout of the second meeting of the exploratory committee for the seismic disaster of Makinohara district of Tomei Expressway, September 28, 2009. (in Japanese)
- Dewoolker, M. M., Ko, H.-Y., Stadler, A. T. and Astaneh, S. M. F., Substitute pore fluid for seismic centrifugal modeling, *Geotechnical Testing Journal*, ASTM, Vol. 22, No. 3, pp. 196-210, 1999.
- Esposito, G., Centrifuge simulation of light hydrocarbon spill in partially saturated Dutch Dune Sand, *Bulletin of Engineering Geology and the Environment*, Vol. 58, No. 2, pp. 89-93, 2000.
- Hayashi, H., Nishikawa, J., and Egawa, T., Earthquake resistance of road embankments under influence of seepage, *Physical Modelling in Geotechnics-ICPMG '02*, Proceedings of the International Conference on Physical Modelling in Geotechnics, St. John's, Newfoundland, Canada, 10-12 July, 2002, Phillips, R., Guo, P. and Popescu, R., eds., Balkema, pp. 483-488, 2002.
- Heibrock, G. and Rezzoug, A., Theoretical and experimental approaches on capillary rise in centrifuge

- 552 modeling, Proc. Int. Conf. Centrifuge 98, Spec. Lecture. Rep., Kimura, T., Kusakabe, O.,
553 Takemura, J. eds., Balkema, pp. 964-965, 1998.
- 554 Higo, Y., Oka, F., Kodaka, T., and Kimoto, S. (2006), Three dimensional strain localization of water-
555 saturated clay and numerical simulation using an elasto-viscoplastic model, *Philosophical*
556 *Magazine*, Structure and Properties of Condensed Matter, 86, 21-22, pp. 3205-3240.
- 557 Japan Road Association, Guidelines for road earthwork, Embankment construction, 2010.
- 558 Ko, H.-Y. and Dewoolker, M.M., Modeling liquefaction in centrifuges, Proc. Int. Workshop on the
559 Physics and Mechanics of Soil Liquefaction, Baltimore, Maryland, USA, September 10-11, Lade,
560 P.V. and Yamamura, J., eds., Balkema, Rotterdam, pp. 307-322, 1999.
- 561 Kodaka, T., Higo, Y. and Takyu, T. (2001), Deformation and failure characteristics of rectangular clay
562 specimens under three-dimensional condition, Proceedings of The 15th International Conference
563 on Soil Mechanics and Geotechnical Engineering, August 27-31, Istanbul, Turkey, pp. 167-170.
- 564 Nakamura, H., Yokota, S., Yasuda, S., Strength and deformation characteristic of expressway banking
565 materials on the Suruga-wan earthquake, the 45th annual meeting of Japanese Geotechnical
566 Society, Matsuyama, D-06, No. 748, pp. 1495-1496, 2010. (in Japanese)
- 567 National Astronomical Observatory editor, Chronological Scientific Tables, Maruzen, Tokyo, p. 375-
568 376, 2001. (in Japanese)
- 569 National Institute for Land and Infrastructure Management Ministry of Land, Infrastructure, Transport
570 and Tourism, Japan (NILIM), and Incorporated Administrative Agency Public Works Research
571 Institute (PWRI), Report on Damage to Infrastructures by the 2004 Mid Niigata Prefecture
572 Earthquake, pp. 157-236, 2004. (in Japanese)
- 573 National Institute for Land and Infrastructure Management Ministry of Land, Infrastructure, Transport
574 and Tourism, Japan (NILIM), Incorporated Administrative Agency Public Works Research
575 Institute (PWRI), and Incorporated Administrative Agency Building Research Institute (BRI),

- 576 Report on damage to infrastructures and buildings by the 2007 Noto Hanto Earthquake, pp. 102-
577 183, 2008. (in Japanese)
- 578 National Institute for Land and Infrastructure Management Ministry of Land, Infrastructure, Transport
579 and Tourism, Japan (NILIM), and Incorporated Administrative Agency Public Works Research
580 Institute (PWRI), Quick report on damage to infrastructures by the 2011 off the Pacific coast of
581 Tohoku Earthquake, pp. 463-485, 2011. (in Japanese)
- 582 Matsuo, O., Saito, Y., Sasaki, T., Kondoh, K., and Sato, T., Earthquake-induced flow slides of fills and
583 infinite slopes, *Soils and Foundations*, Vol. 42, No. 1, pp. 89-104, 2002.
- 584 Ohkawa, H., Sugita, H., Sasaki, T. and Mizuhashi, M., Dynamic Centrifuge Model Tests on earthquake
585 resistant characteristics of mountain road fill, The 43rd annual meeting of JGS, Hiroshima, July
586 9-12, CD-ROM, H-06, No. 572, pp. 1143-1144, 2008. (in Japanese)
- 587 Okamura, M. and Tamamura, S., Seismic stability of embankment on soft soil deposit, *International*
588 *Journal of Physical Modelling in Geotechnics*, Vol. 11, Issue 2, pp. 50-57, 2011.
- 589 Okamura, M., Tamamura, S. and Yamamoto, R., Seismic stability of embankments subjected to pre-
590 deformation due to foundation consolidation, *Soils and Foundations*, Vol. 53, No. 1, pp.11-22,
591 2013.
- 592 Rezzoug, A., König, D. and Triantafyllidis, T., Scaling laws for centrifuge modeling of capillary rise
593 in sandy soils, *Journal of Geotechnical and Geoenvironmental Engineering*, ASCE, Vol. 130, pp.
594 615-620, 2000.
- 595 Sakai, Y., Reinvestigation on period range of strong ground motions corresponding to buildings
596 damage, including data of the 2007 Noto-Hanto and Niigata-ken Chuetsu-Oki Earthquakes,
597 Journal of structure and construction engineering, Architectural Institute of Japan, Vol. 74, No.
598 642, pp. 1531-1536, 2009. (in Japanese)
- 599 Sasaki, T., Sugita, H., Ohkawa, H. and Mizuhashi, M., Ground investigation of the embankments

- 600 damaged by the 2007 Noto Hanto Earthquake, the 63rd annual meeting of JSCE, Sendai,
601 September 10-20, CD-ROM, disc1, 3-034, pp. 67-68, 2008. (in Japanese)
- 602 Thorel, L., Ferber, V., Caicedo, B. and Khokhar, I.M., Physical modelling of wetting-induced collapse
603 in embankment base, *Géotechnique*, Vol. 61, No. 5, pp. 409-420, 2013

List of Tables and Figures

Table 1 : Specifications of centrifugal model test machine

Table 2 : Specifications of shaking table

Table 3 : Material properties of Yodogawa-levee sand

Table 4 : Test cases with different water contents

Figure 1 : Schematic figure of geotechnical centrifuge machine at DPRI, Kyoto University

Figure 2 : Schematic figure of shaking table

Figure 3 : Grain size cumulative curve of Yodogawa-levee sand

Figure 4 : Compaction curve of Yodogawa-levee sand

Figure 5 : Model container and model embankment

Figure 6 : Preparation of model embankment

Figure 7 : Location and size of soil samples in model scale for measuring water contents after tests

Figure 8: Distribution of water contents

Figure 9 : Relation between degree of saturation and suction measured by tensiometer

Figure 10 : Input and output dynamic loads-time profile

Figure 11 : Displacements for Case 1, Case 2 and Case 3: (a) Time histories of displacement during dynamic loading process; (b) Displacement before shaking and after dynamic loading process; and (c) Displacement vectors

Figure 12 : Distributions of shear strain γ and volumetric strain ϵ_v with $\epsilon_v = 0$ line

Figure 13 : Time histories of pore water pressure of each measuring point

Figure 14 : Acceleration responses

Figure 15 : Deformation mode of unsaturated embankment with higher water content (Case 3)

Table 1 Specifications of centrifugal model test machine

Effective rotation radius	2.50 (m)
Effective space for model installation (L × W × H)	800 × 320 × 800 (mm)
Allowable weight of model	120 (kg)
Test capacity	24 (g· ton)
Maximum centrifugal acceleration	200 (g)

Table 2 Specifications of shaking table

Vibration control method	Servo oil pressure control
Allowable centrifugal acceleration	50 (g)
Displacement	±5 (mm)
Maximum frequency	200 (Hz)
Input of waveform	Sine wave Arbitrary wave
Allowable weight of model	100 (kg)

Table 3 Material properties of Yodogawa-levee sand

Sand(%)	74.5
Silt(%)	14.2
Clay(%)	11.3
Maximum particle diameter D_{\max} (mm)	2.0
Average particle diameter D_{50} (mm)	0.28
Particle density ρ_s (g/cm ³)	2.661
Optimum water content w_{opt} (%)	13.7
Maximum dry density ρ_{dmax} (g/cm ³)	1.838

Table 4 Test cases with different water contents

Case no.		Case 1	Case 2	Case 3
Water content (%)	Before compacting w_{bef}	13.5	14.5	18.0
	After testing w_{aft}	12.1	13.5	17.4
Degree of saturation (%)	Before compacting $S_{\text{r bef}}$	61.0	65.5	81.3
	After testing $S_{\text{r aft}}$	54.5	61.2	78.7
Compacted wet density (g/cm ³)**	Before compacting $\rho_{\text{t bef}}$	1.901	1.918	1.977
	After testing $\rho_{\text{t aft}}$	1.878	1.901	1.966
Maximum acceleration of input wave measured at shaking table (gal)		374.6	440.1	424.2

*Optimum water content (w_{opt}) = 13.7%

** Dry density for all cases = 1.675 (g/cm³), corresponding to Dc = 91%.

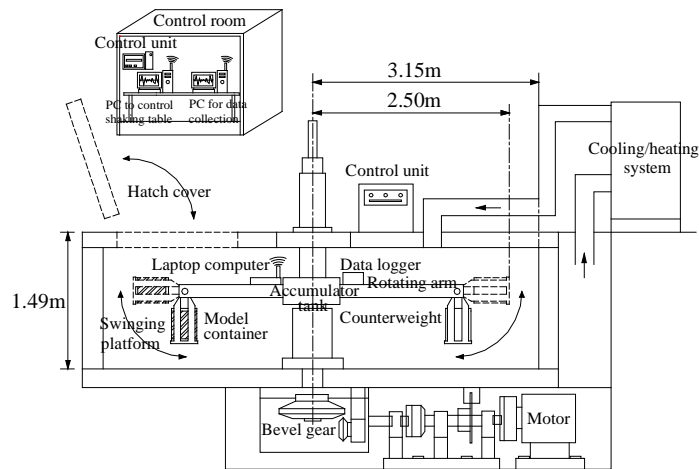


Figure 1 Schematic figure of geotechnical centrifuge machine at DPRI, Kyoto University

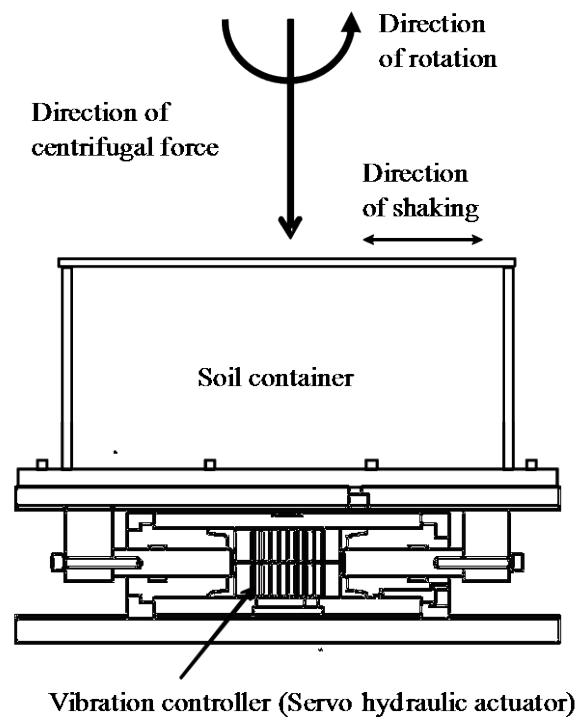


Figure 2 Schematic figure of shaking table

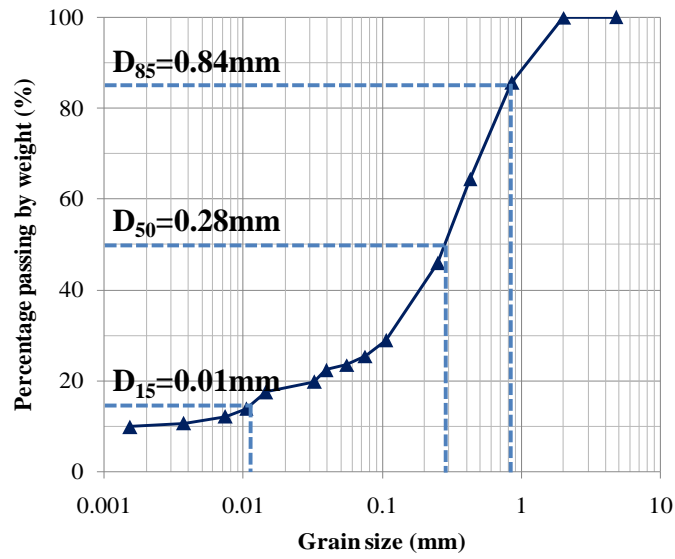


Figure 3 Grain size cumulative curve of Yodogawa-levee sand

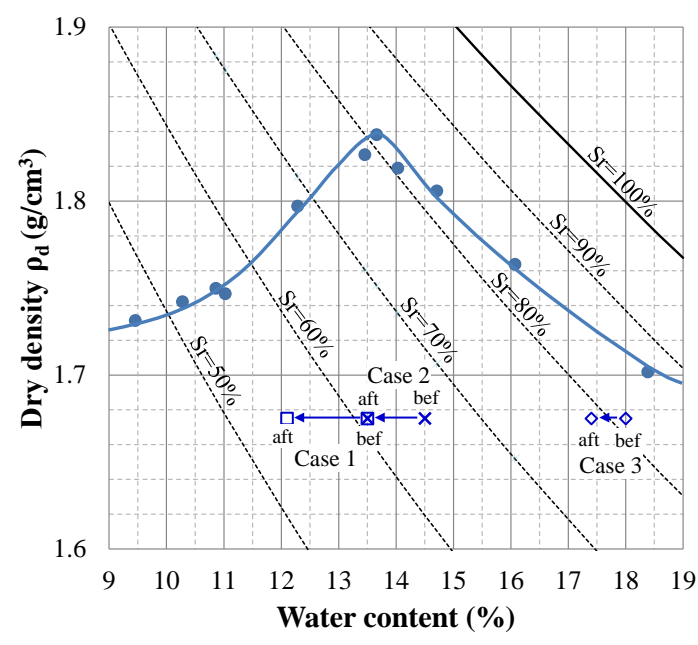
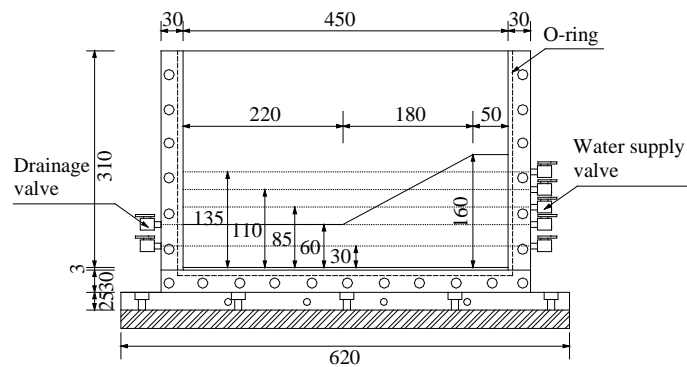
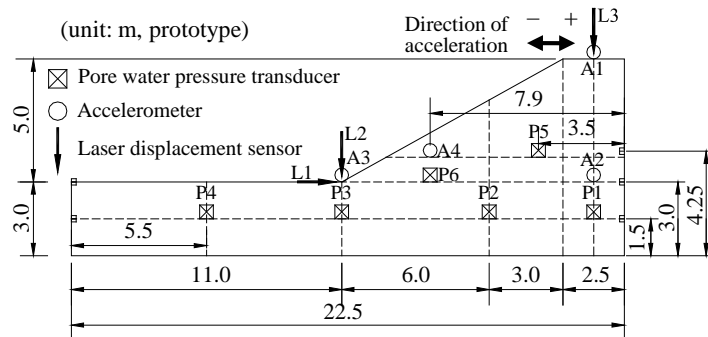


Figure 4 Compaction curve of Yodogawa-levee sand

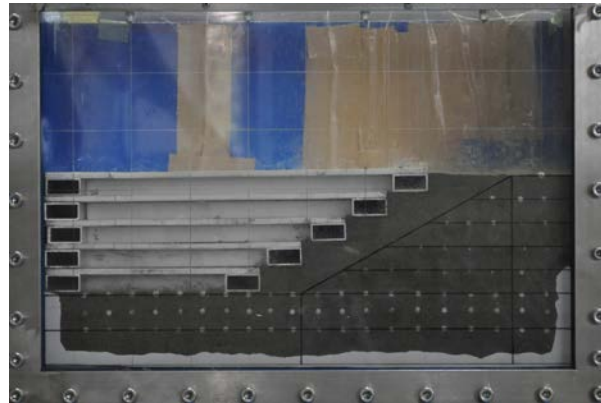


(a) Front view of model container in model scale



(b) Model configuration in prototype scale and sensor locations

Figure 5 Model container and model embankment



(a) Just after completing compaction



(b) Model embankment used for tests

Figure 6 Preparation of model embankment

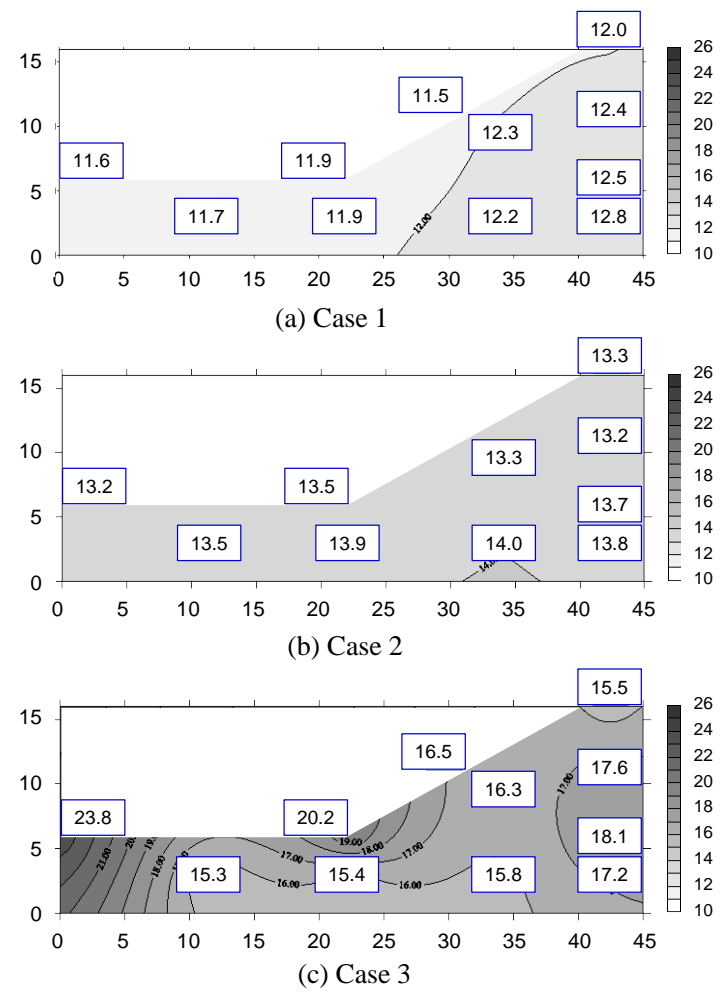


Figure 8 Distribution of water contents

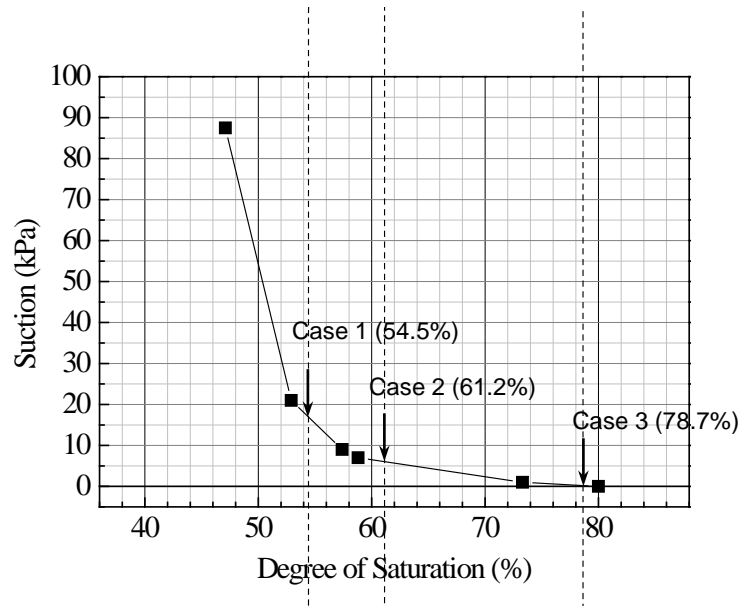
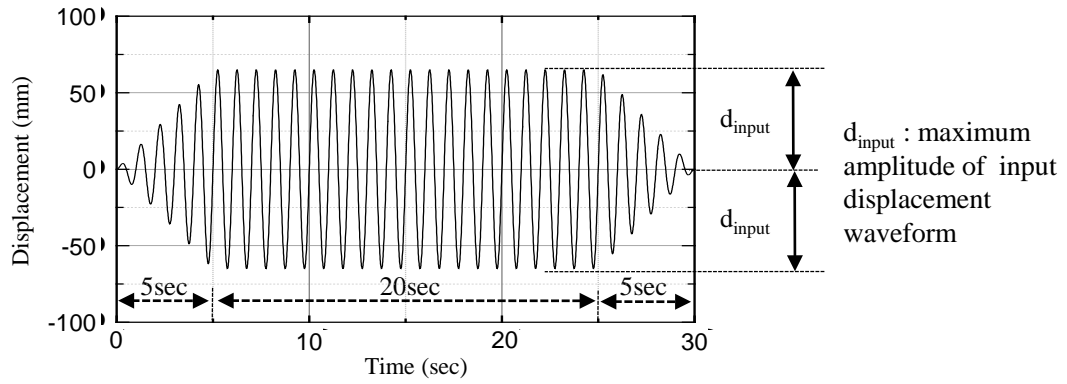
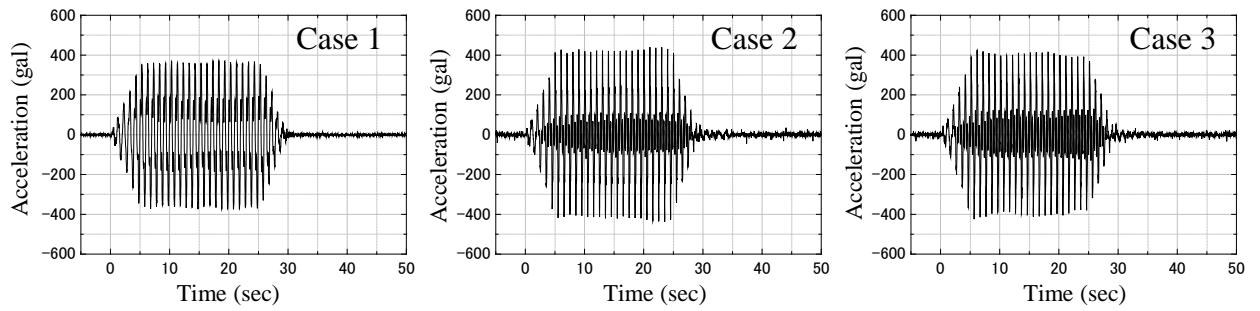


Figure 9 Relation between degree of saturation and suction measured by tensiometer

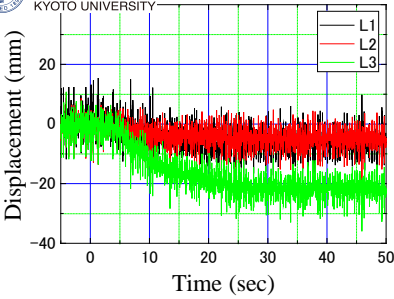


(a) Input displacement waveform

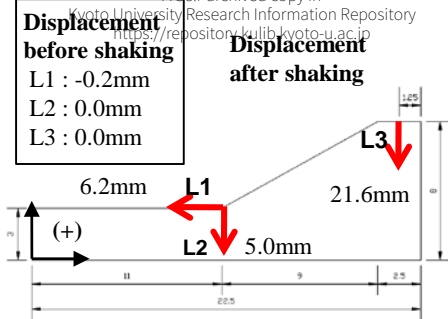


(b) Acceleration waveforms measured at shaking table

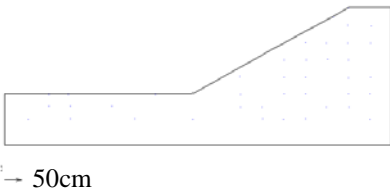
Figure 10 Input and output dynamic loads-time profile



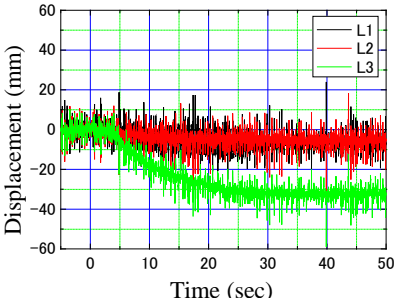
Case 1



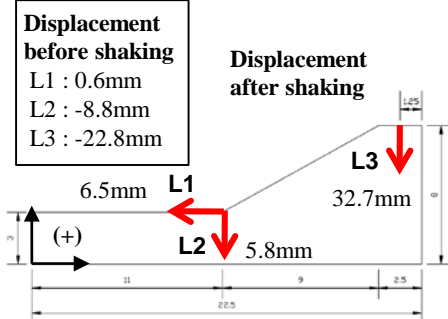
Case 1



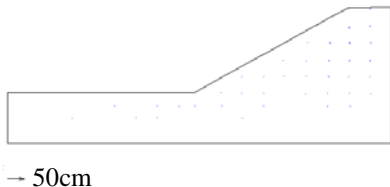
Case 1



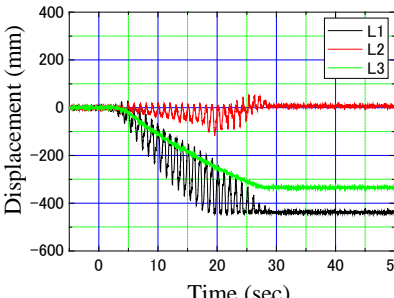
Case 2



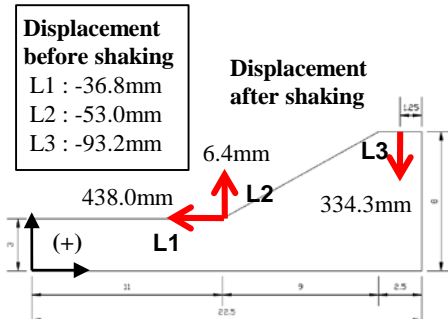
Case 2



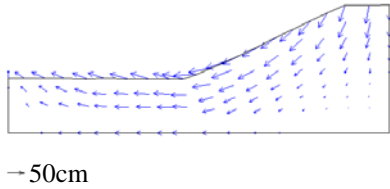
Case 2



Case 3



Case 3



Case 3

Figure 11 Displacements for Case 1, Case 2 and Case 3: (a) Time histories of displacement during dynamic loading process; (b) Displacement before shaking and after dynamic loading process; and (c) Displacement vectors

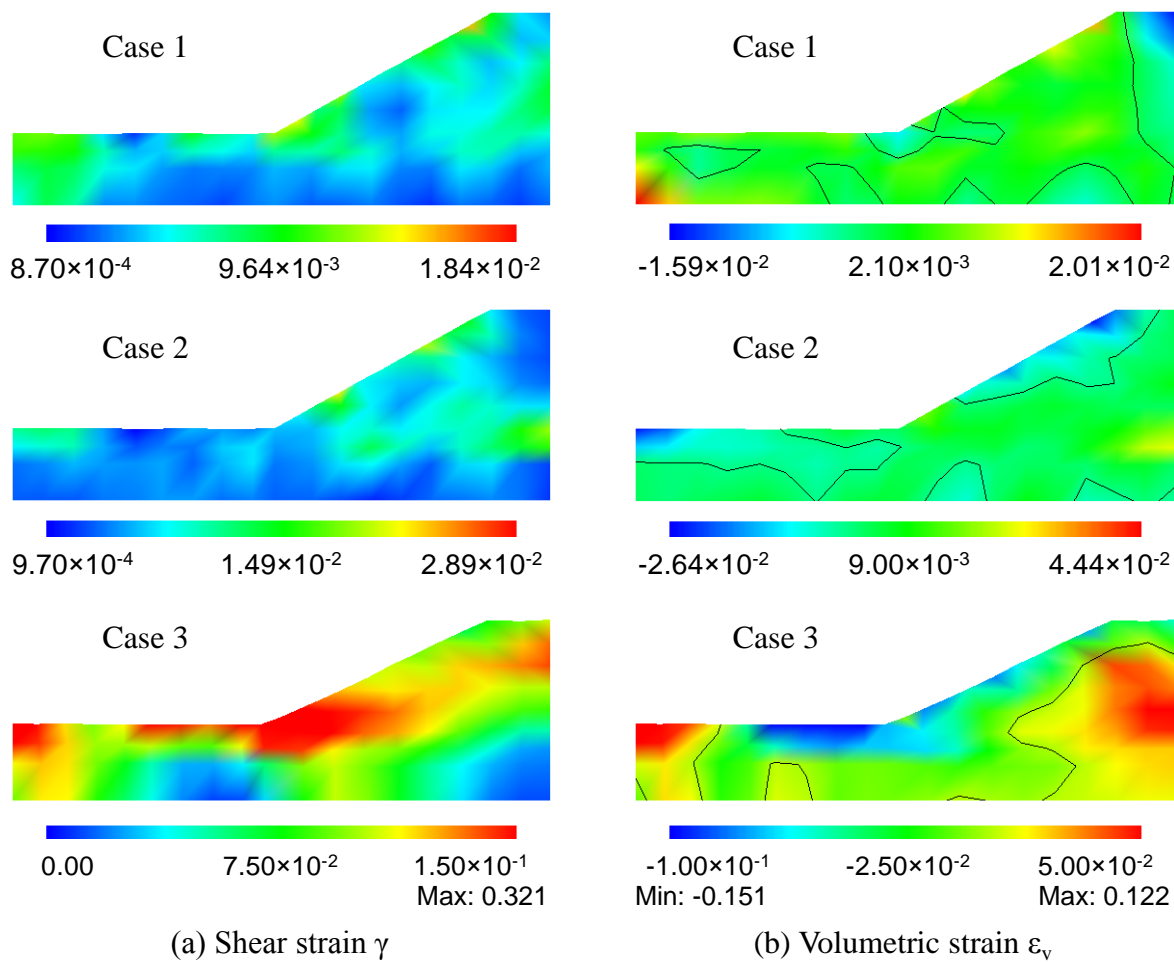
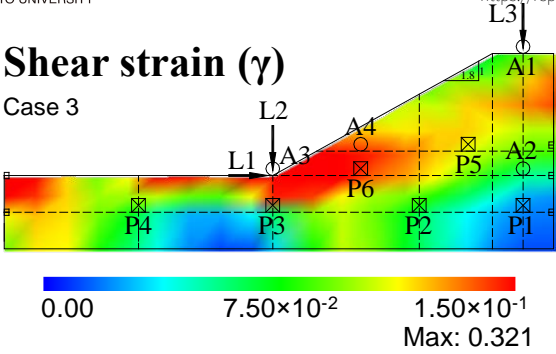


Figure 12 Distributions of shear strain γ and volumetric strain ε_v with $\varepsilon_v=0$ line

Shear strain (γ)

Case 3



Volumetric strain (ϵ_v)

Case 3

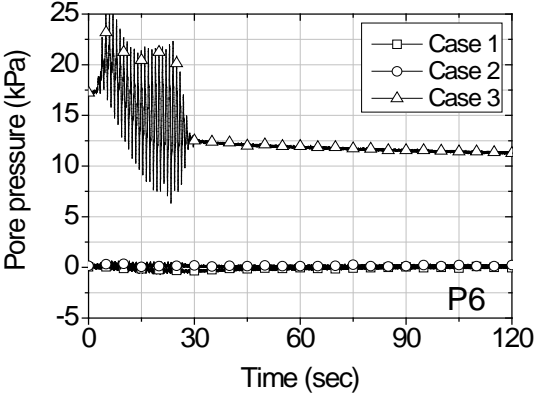
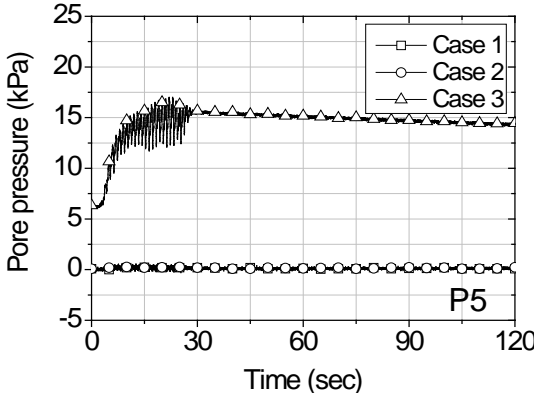
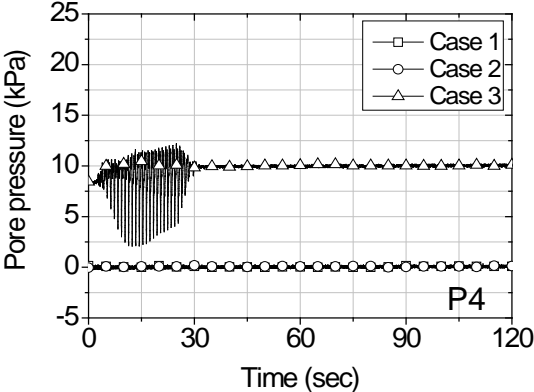
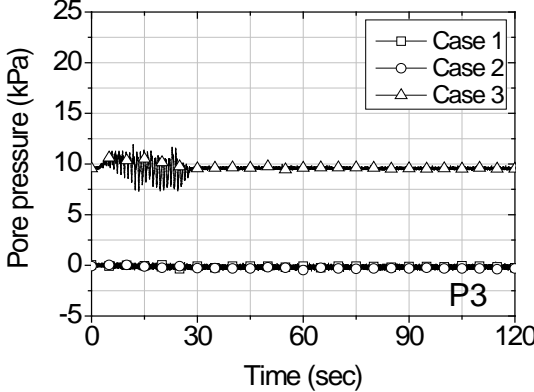
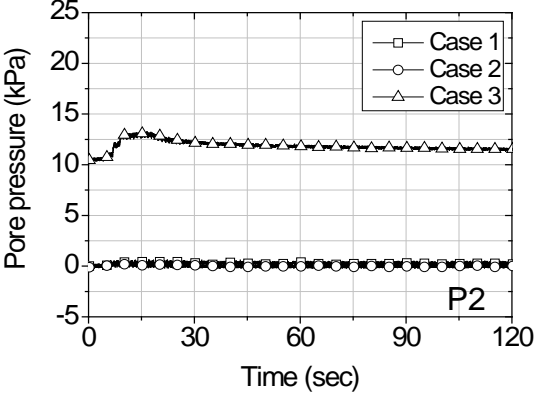
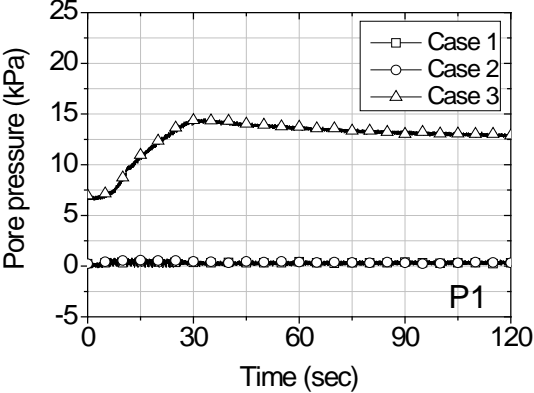
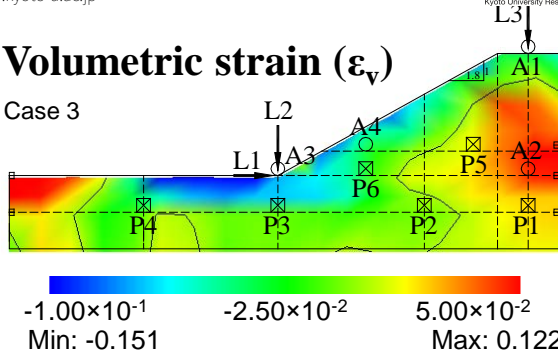


Figure 13 Time histories of pore water pressure of each measuring point

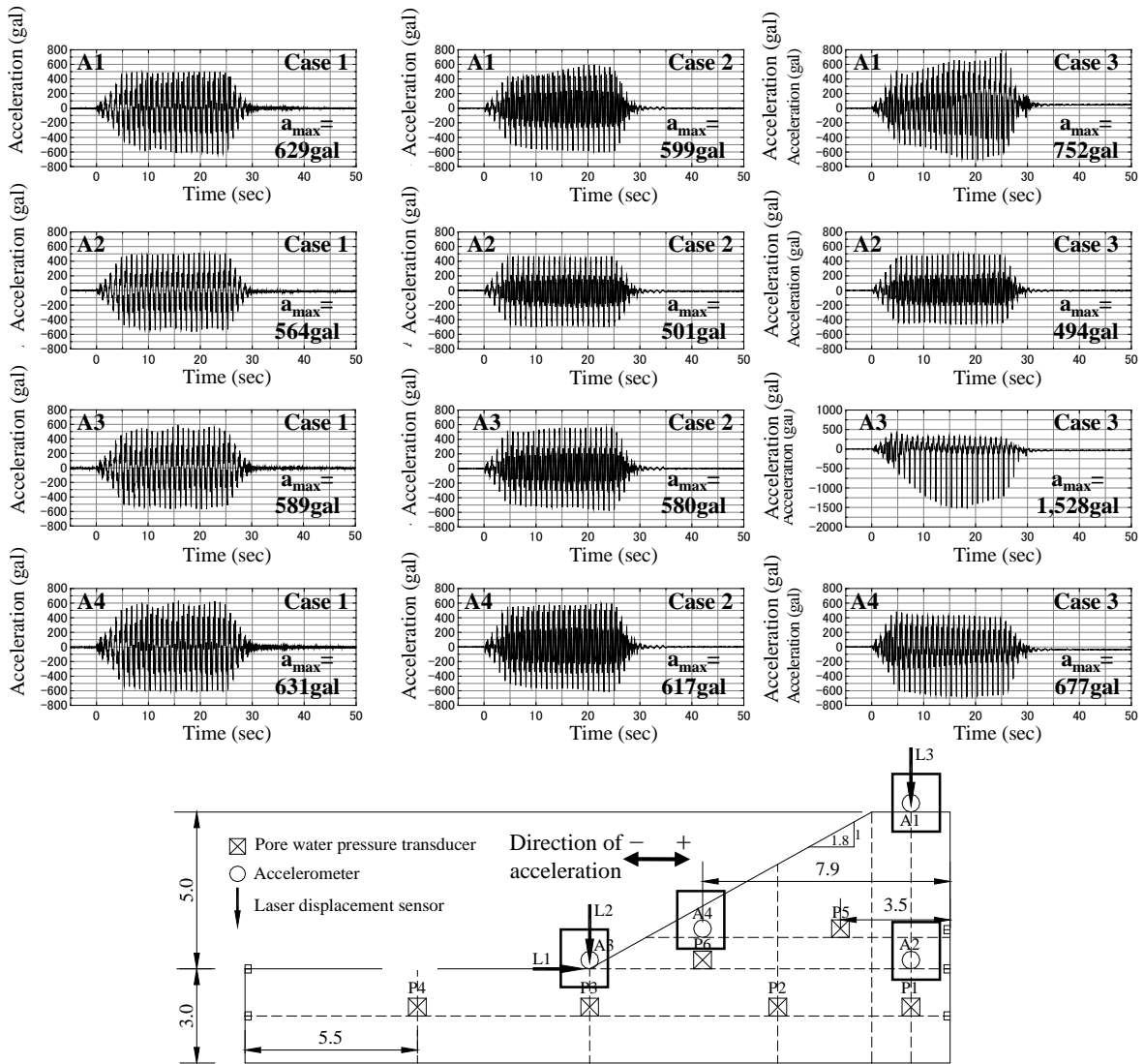


Figure 14 Acceleration responses

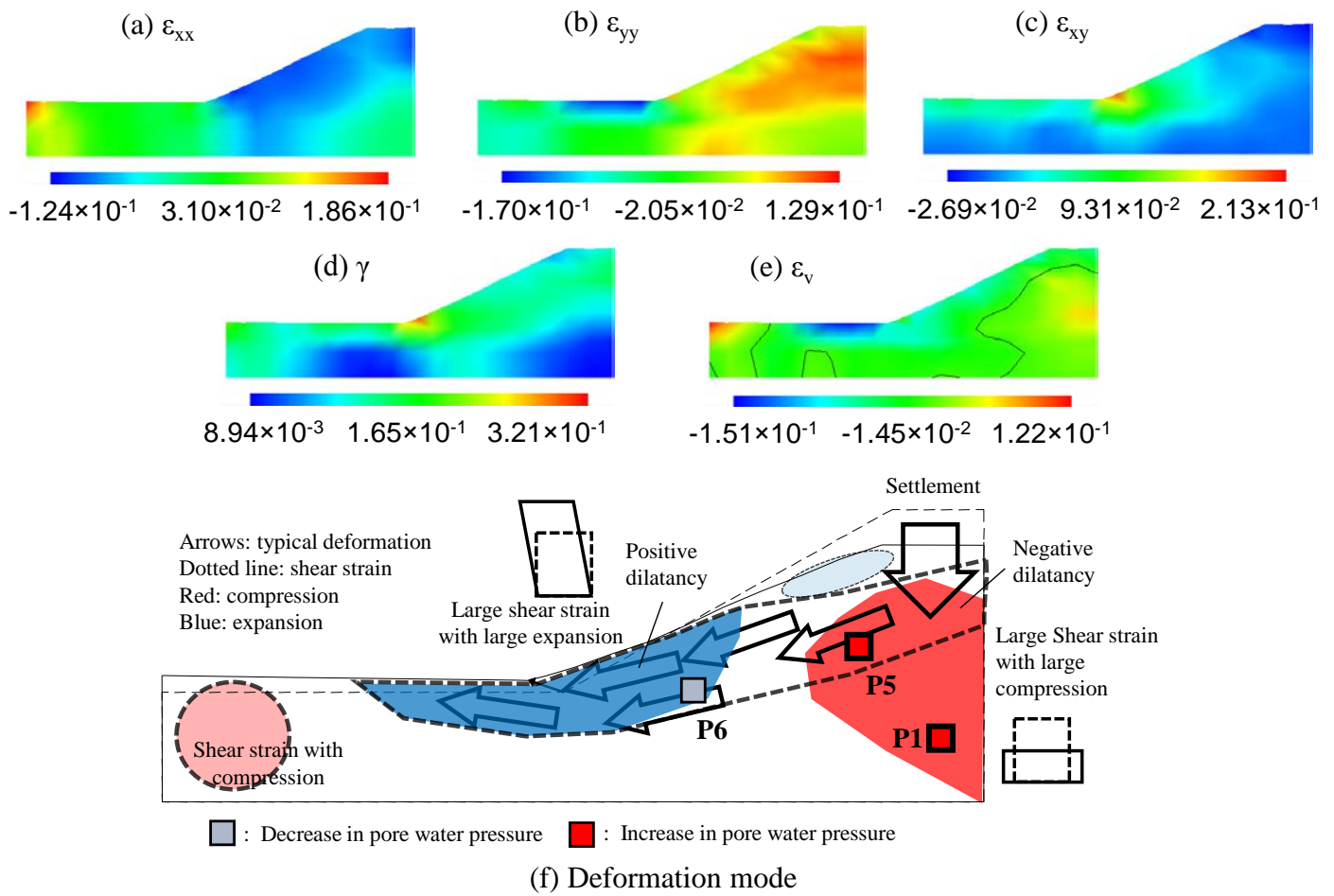


Figure 15 Deformation mode of unsaturated embankment with higher water content (Case 3)